

J/ψ suppression at forward rapidity in Au+Au collisions at $\sqrt{s_{NN}}=200$ GeV

A. Adare,¹¹ S. Afanasiev,²⁷ C. Aidala,⁴⁰ N.N. Ajitanand,⁵⁷ Y. Akiba,^{51,52} H. Al-Bataineh,⁴⁶ J. Alexander,⁵⁷ K. Aoki,^{33,51} Y. Aramaki,¹⁰ E.T. Atomssa,³⁴ R. Averbeck,⁵⁸ T.C. Awes,⁴⁷ B. Azmoun,⁵ V. Babintsev,²² M. Bai,⁴ G. Baksay,¹⁸ L. Baksay,¹⁸ K.N. Barish,⁶ B. Bassalleck,⁴⁵ A.T. Basye,¹ S. Bathe,⁶ V. Baublis,⁵⁰ C. Baumann,⁴¹ A. Bazilevsky,⁵ S. Belikov,^{5,*} R. Belmont,⁶² R. Bennett,⁵⁸ A. Berdnikov,⁵⁴ Y. Berdnikov,⁵⁴ A.A. Bickley,¹¹ J.S. Bok,⁶⁵ K. Boyle,⁵⁸ M.L. Brooks,³⁶ H. Buesching,⁵ V. Bumazhnov,²² G. Bunce,^{5,52} S. Butsyk,³⁶ C.M. Camacho,³⁶ S. Campbell,⁵⁸ C.-H. Chen,⁵⁸ C.Y. Chi,¹² M. Chiu,⁵ I.J. Choi,⁶⁵ R.K. Choudhury,³ P. Christiansen,³⁸ T. Chujo,⁶¹ P. Chung,⁵⁷ O. Chvala,⁶ V. Cianciolo,⁴⁷ Z. Citron,⁵⁸ B.A. Cole,¹² M. Connors,⁵⁸ P. Constantin,³⁶ M. Csanád,¹⁶ T. Csörgő,³⁰ T. Dahms,⁵⁸ S. Dairaku,^{33,51} I. Danchev,⁶² K. Das,¹⁹ A. Datta,⁴⁰ G. David,⁵ A. Denisov,²² A. Deshpande,^{52,58} E.J. Desmond,⁵ O. Dietzsch,⁵⁵ A. Dion,⁵⁸ M. Donadelli,⁵⁵ O. Drapier,³⁴ A. Drees,⁵⁸ K.A. Drees,⁴ J.M. Durham,⁵⁸ A. Durum,²² D. Dutta,³ S. Edwards,¹⁹ Y.V. Efremenko,⁴⁷ F. Ellinghaus,¹¹ T. Engelmore,¹² A. Enokizono,³⁵ H. En'yo,^{51,52} S. Esumi,⁶¹ B. Fadem,⁴² D.E. Fields,⁴⁵ M. Finger, Jr.,⁷ M. Finger,⁷ F. Fleuret,³⁴ S.L. Fokin,³² Z. Fraenkel,^{64,*} J.E. Frantz,⁵⁸ A. Franz,⁵ A.D. Frawley,¹⁹ K. Fujiwara,⁵¹ Y. Fukao,⁵¹ T. Fusayasu,⁴⁴ I. Garishvili,⁵⁹ A. Glenn,¹¹ H. Gong,⁵⁸ M. Gonin,³⁴ Y. Goto,^{51,52} R. Granier de Cassagnac,³⁴ N. Grau,¹² S.V. Greene,⁶² M. Grosse Perdekamp,^{23,52} T. Gunji,¹⁰ H.-Å. Gustafsson,^{38,*} J.S. Haggerty,⁵ K.I. Hahn,¹⁷ H. Hamagaki,¹⁰ J. Hamblen,⁵⁹ J. Hanks,¹² R. Han,⁴⁹ E.P. Hartouni,³⁵ E. Haslum,³⁸ R. Hayano,¹⁰ M. Heffner,³⁵ T.K. Hemmick,⁵⁸ T. Hester,⁶ X. He,²⁰ J.C. Hill,²⁶ M. Hohlmann,¹⁸ W. Holzmann,¹² K. Homma,²¹ B. Hong,³¹ T. Horaguchi,²¹ D. Hornback,⁵⁹ S. Huang,⁶² T. Ichihara,^{51,52} R. Ichimiya,⁵¹ J. Ide,⁴² Y. Ikeda,⁶¹ K. Imai,^{33,51} M. Inaba,⁶¹ D. Isenhower,¹ M. Ishihara,⁵¹ T. Isobe,¹⁰ M. Issah,⁶² A. Isupov,²⁷ D. Ivanischev,⁵⁰ B.V. Jacak,^{58,†} J. Jia,^{5,57} J. Jin,¹² B.M. Johnson,⁵ K.S. Joo,⁴³ D. Jouan,⁴⁸ D.S. Jumper,¹ F. Kajihara,¹⁰ S. Kametani,⁵¹ N. Kamihara,⁵² J. Kamin,⁵⁸ J.H. Kang,⁶⁵ J. Kapustinsky,³⁶ K. Karatsu,³³ D. Kawall,^{40,52} M. Kawashima,^{53,51} A.V. Kazantsev,³² T. Kempel,²⁶ A. Khanzadeev,⁵⁰ K.M. Kijima,²¹ B.I. Kim,³¹ D.H. Kim,⁴³ D.J. Kim,²⁸ E.J. Kim,⁸ E. Kim,⁵⁶ S.H. Kim,⁶⁵ Y.J. Kim,²³ E. Kinney,¹¹ K. Kiriluk,¹¹ Á. Kiss,¹⁶ E. Kistenev,⁵ L. Kochenda,⁵⁰ B. Komkov,⁵⁰ M. Konno,⁶¹ J. Koster,²³ D. Kotchetkov,⁴⁵ A. Kozlov,⁶⁴ A. Král,¹³ A. Kravitz,¹² G.J. Kunde,³⁶ K. Kurita,^{53,51} M. Kurosawa,⁵¹ Y. Kwon,⁶⁵ G.S. Kyle,⁴⁶ R. Lacey,⁵⁷ Y.S. Lai,¹² J.G. Lajoie,²⁶ A. Lebedev,²⁶ D.M. Lee,³⁶ J. Lee,¹⁷ K.B. Lee,³¹ K. Lee,⁵⁶ K.S. Lee,³¹ M.J. Leitch,³⁶ M.A.L. Leite,⁵⁵ E. Leitner,⁶² B. Lenzi,⁵⁵ P. Liebing,⁵² L.A. Linden Levy,¹¹ T. Liška,¹³ A. Litvinenko,²⁷ H. Liu,^{36,46} M.X. Liu,³⁶ X. Li,⁹ B. Love,⁶² R. Luechtenborg,⁴¹ D. Lynch,⁵ C.F. Maguire,⁶² Y.I. Makdisi,⁴ A. Malakhov,²⁷ M.D. Malik,⁴⁵ V.I. Manko,³² E. Mannel,¹² Y. Mao,^{49,51} H. Masui,⁶¹ F. Matathias,¹² M. McCumber,⁵⁸ P.L. McGaughey,³⁶ N. Means,⁵⁸ B. Meredith,²³ Y. Miake,⁶¹ A.C. Mignerey,³⁹ P. Mikeš,^{7,25} K. Miki,⁶¹ A. Milov,⁵ M. Mishra,² J.T. Mitchell,⁵ A.K. Mohanty,³ Y. Morino,¹⁰ A. Morreale,⁶ D.P. Morrison,⁵ T.V. Moukhanova,³² J. Murata,^{53,51} S. Nagamiya,²⁹ J.L. Nagle,¹¹ M. Naglis,⁶⁴ M.I. Nagy,¹⁶ I. Nakagawa,^{51,52} Y. Nakamiya,²¹ T. Nakamura,^{21,29} K. Nakano,^{51,60} J. Newby,³⁵ M. Nguyen,⁵⁸ R. Nouicer,⁵ A.S. Nyanin,³² E. O'Brien,⁵ S.X. Oda,¹⁰ C.A. Ogilvie,²⁶ K. Okada,⁵² M. Oka,⁶¹ Y. Onuki,⁵¹ A. Oskarsson,³⁸ M. Ouchida,²¹ K. Ozawa,¹⁰ R. Pak,⁵ V. Pantuev,^{24,58} V. Papavassiliou,⁴⁶ I.H. Park,¹⁷ J. Park,⁵⁶ S.K. Park,³¹ W.J. Park,³¹ S.F. Pate,⁴⁶ H. Pei,²⁶ J.-C. Peng,²³ H. Pereira,¹⁴ V. Peresedov,²⁷ D.Yu. Peressounko,³² C. Pinkenburg,⁵ R.P. Pisani,⁵ M. Proissl,⁵⁸ M.L. Purschke,⁵ A.K. Purwar,³⁶ H. Qu,²⁰ J. Rak,²⁸ A. Rakotozafindrabe,³⁴ I. Ravinovich,⁶⁴ K.F. Read,^{47,59} K. Reygers,⁴¹ V. Riabov,⁵⁰ Y. Riabov,⁵⁰ E. Richardson,³⁹ D. Roach,⁶² G. Roche,³⁷ S.D. Rolnick,⁶ M. Rosati,²⁶ C.A. Rosen,¹¹ S.S.E. Rosendahl,³⁸ P. Rosnet,³⁷ P. Rukoyatkin,²⁷ P. Ružička,²⁵ B. Sahlmueller,⁴¹ N. Saito,²⁹ T. Sakaguchi,⁵ K. Sakashita,^{51,60} V. Samsonov,⁵⁰ S. Sano,^{10,63} T. Sato,⁶¹ S. Sawada,²⁹ K. Sedgwick,⁶ J. Seele,¹¹ R. Seidl,²³ A.Yu. Semenov,²⁶ R. Seto,⁶ D. Sharma,⁶⁴ I. Shein,²² T.-A. Shibata,^{51,60} K. Shigaki,²¹ M. Shimomura,⁶¹ K. Shoji,^{33,51} P. Shukla,³ A. Sickles,⁵ C.L. Silva,⁵⁵ D. Silvermyr,⁴⁷ C. Silvestre,¹⁴ K.S. Sim,³¹ B.K. Singh,² C.P. Singh,² V. Singh,² M. Slunečka,⁷ R.A. Soltz,³⁵ W.E. Sondheim,³⁶ S.P. Sorensen,⁵⁹ I.V. Sourikova,⁵ N.A. Sparks,¹ P.W. Stankus,⁴⁷ E. Stenlund,³⁸ S.P. Stoll,⁵ T. Sugitate,²¹ A. Sukhanov,⁵ J. Sziklai,³⁰ E.M. Takagui,⁵⁵ A. Taketani,^{51,52} R. Tanabe,⁶¹ Y. Tanaka,⁴⁴ K. Tanida,^{33,51,52} M.J. Tannenbaum,⁵ S. Tarafdar,² A. Taranenko,⁵⁷ P. Tarján,¹⁵ H. Themann,⁵⁸ T.L. Thomas,⁴⁵ M. Togawa,^{33,51} A. Toia,⁵⁸ L. Tomášek,²⁵ H. Torii,²¹ R.S. Towell,¹ I. Tserruya,⁶⁴ Y. Tsuchimoto,²¹ C. Vale,^{5,26} H. Valle,⁶² H.W. van Hecke,³⁶ E. Vazquez-Zambrano,¹² A. Veicht,²³ J. Velkovska,⁶² R. Vértesi,^{15,30} A.A. Vinogradov,³² M. Virius,¹³ V. Vrba,²⁵ E. Vznuzdaev,⁵⁰ X.R. Wang,⁴⁶ D. Watanabe,²¹ K. Watanabe,⁶¹ Y. Watanabe,^{51,52} F. Wei,²⁶ R. Wei,⁵⁷ J. Wessels,⁴¹ S.N. White,⁵ D. Winter,¹² J.P. Wood,¹ C.L. Woody,⁵ R.M. Wright,¹ M. Wysocki,¹¹ W. Xie,⁵² Y.L. Yamaguchi,¹⁰ K. Yamaura,²¹ R. Yang,²³ A. Yanovich,²² J. Ying,²⁰ S. Yokkaichi,^{51,52} G.R. Young,⁴⁷ I. Younus,⁴⁵ Z. You,⁴⁹ I.E. Yushmanov,³² W.A. Zajc,¹² C. Zhang,⁴⁷ S. Zhou,⁹ and L. Zolin²⁷

(PHENIX Collaboration)

- ¹Abilene Christian University, Abilene, Texas 79699, USA
²Department of Physics, Banaras Hindu University, Varanasi 221005, India
³Bhabha Atomic Research Centre, Bombay 400 085, India
⁴Collider-Accelerator Department, Brookhaven National Laboratory, Upton, New York 11973-5000, USA
⁵Physics Department, Brookhaven National Laboratory, Upton, New York 11973-5000, USA
⁶University of California - Riverside, Riverside, California 92521, USA
⁷Charles University, Ovocný trh 5, Praha 1, 116 36, Prague, Czech Republic
⁸Chonbuk National University, Jeonju, 561-756, Korea
⁹China Institute of Atomic Energy (CIAE), Beijing, People's Republic of China
¹⁰Center for Nuclear Study, Graduate School of Science, University of Tokyo, 7-3-1 Hongo, Bunkyo, Tokyo 113-0033, Japan
¹¹University of Colorado, Boulder, Colorado 80309, USA
¹²Columbia University, New York, New York 10027 and Nevis Laboratories, Irvington, New York 10533, USA
¹³Czech Technical University, Zikova 4, 166 36 Prague 6, Czech Republic
¹⁴Dapnia, CEA Saclay, F-91191, Gif-sur-Yvette, France
¹⁵Debrecen University, H-4010 Debrecen, Egyetem tér 1, Hungary
¹⁶ELTE, Eötvös Loránd University, H - 1117 Budapest, Pázmány P. s. 1/A, Hungary
¹⁷Ewha Womans University, Seoul 120-750, Korea
¹⁸Florida Institute of Technology, Melbourne, Florida 32901, USA
¹⁹Florida State University, Tallahassee, Florida 32306, USA
²⁰Georgia State University, Atlanta, Georgia 30303, USA
²¹Hiroshima University, Kagamiyama, Higashi-Hiroshima 739-8526, Japan
²²IHEP Protvino, State Research Center of Russian Federation, Institute for High Energy Physics, Protvino, 142281, Russia
²³University of Illinois at Urbana-Champaign, Urbana, Illinois 61801, USA
²⁴Institute for Nuclear Research of the Russian Academy of Sciences, prospekt 60-letiya Oktyabrya 7a, Moscow 117312, Russia
²⁵Institute of Physics, Academy of Sciences of the Czech Republic, Na Slovance 2, 182 21 Prague 8, Czech Republic
²⁶Iowa State University, Ames, Iowa 50011, USA
²⁷Joint Institute for Nuclear Research, 141980 Dubna, Moscow Region, Russia
²⁸Helsinki Institute of Physics and University of Jyväskylä, P.O.Box 35, FI-40014 Jyväskylä, Finland
²⁹KEK, High Energy Accelerator Research Organization, Tsukuba, Ibaraki 305-0801, Japan
³⁰KFKI Research Institute for Particle and Nuclear Physics of the Hungarian Academy of Sciences (MTA KFKI RMKI), H-1525 Budapest 114, POBox 49, Budapest, Hungary
³¹Korea University, Seoul, 136-701, Korea
³²Russian Research Center "Kurchatov Institute", Moscow, 123098 Russia
³³Kyoto University, Kyoto 606-8502, Japan
³⁴Laboratoire Leprince-Ringuet, Ecole Polytechnique, CNRS-IN2P3, Route de Saclay, F-91128, Palaiseau, France
³⁵Lawrence Livermore National Laboratory, Livermore, California 94550, USA
³⁶Los Alamos National Laboratory, Los Alamos, New Mexico 87545, USA
³⁷LPC, Université Blaise Pascal, CNRS-IN2P3, Clermont-Fd, 63177 Aubiere Cedex, France
³⁸Department of Physics, Lund University, Box 118, SE-221 00 Lund, Sweden
³⁹University of Maryland, College Park, Maryland 20742, USA
⁴⁰Department of Physics, University of Massachusetts, Amherst, Massachusetts 01003-9337, USA
⁴¹Institut für Kernphysik, University of Muenster, D-48149 Muenster, Germany
⁴²Muhlenberg College, Allentown, Pennsylvania 18104-5586, USA
⁴³Myongji University, Yongin, Kyonggido 449-728, Korea
⁴⁴Nagasaki Institute of Applied Science, Nagasaki-shi, Nagasaki 851-0193, Japan
⁴⁵University of New Mexico, Albuquerque, New Mexico 87131, USA
⁴⁶New Mexico State University, Las Cruces, New Mexico 88003, USA
⁴⁷Oak Ridge National Laboratory, Oak Ridge, Tennessee 37831, USA
⁴⁸IPN-Orsay, Université Paris Sud, CNRS-IN2P3, BP1, F-91406, Orsay, France
⁴⁹Peking University, Beijing, People's Republic of China
⁵⁰PNPI, Petersburg Nuclear Physics Institute, Gatchina, Leningrad region, 188300, Russia
⁵¹RIKEN Nishina Center for Accelerator-Based Science, Wako, Saitama 351-0198, Japan
⁵²RIKEN BNL Research Center, Brookhaven National Laboratory, Upton, New York 11973-5000, USA
⁵³Physics Department, Rikkyo University, 3-34-1 Nishi-Ikebukuro, Toshima, Tokyo 171-8501, Japan
⁵⁴Saint Petersburg State Polytechnic University, St. Petersburg, 195251 Russia
⁵⁵Universidade de São Paulo, Instituto de Física, Caixa Postal 66318, São Paulo CEP05315-970, Brazil
⁵⁶Seoul National University, Seoul, Korea
⁵⁷Chemistry Department, Stony Brook University, SUNY, Stony Brook, New York 11794-3400, USA
⁵⁸Department of Physics and Astronomy, Stony Brook University, SUNY, Stony Brook, New York 11794-3400, USA
⁵⁹University of Tennessee, Knoxville, Tennessee 37996, USA
⁶⁰Department of Physics, Tokyo Institute of Technology, Oh-okayama, Meguro, Tokyo 152-8551, Japan
⁶¹Institute of Physics, University of Tsukuba, Tsukuba, Ibaraki 305, Japan

⁶²*Vanderbilt University, Nashville, Tennessee 37235, USA*
⁶³*Waseda University, Advanced Research Institute for Science and
Engineering, 17 Kikui-cho, Shinjuku-ku, Tokyo 162-0044, Japan*
⁶⁴*Weizmann Institute, Rehovot 76100, Israel*
⁶⁵*Yonsei University, IPAP, Seoul 120-749, Korea*
(Dated: August 14, 2019)

Heavy quarkonia are observed to be suppressed in relativistic heavy ion collisions relative to their production in $p+p$ collisions scaled by the number of binary collisions. In order to determine if this suppression is related to color screening of these states in the produced medium, one needs to account for other nuclear modifications including those in cold nuclear matter. In this paper, we present new measurements from the PHENIX 2007 data set of J/ψ yields at forward rapidity ($1.2 < |y| < 2.2$) in Au+Au collisions at $\sqrt{s_{NN}} = 200$ GeV. The data confirm the earlier finding that the suppression of J/ψ at forward rapidity is stronger than at midrapidity, while also extending the measurement to finer bins in collision centrality and higher transverse momentum (p_T). We compare the experimental data to the most recent theoretical calculations that incorporate a variety of physics mechanisms including gluon saturation, gluon shadowing, initial-state parton energy loss, cold nuclear matter breakup, color screening, and charm recombination. We find J/ψ suppression beyond cold-nuclear-matter effects. However, the current level of disagreement between models and d +Au data precludes using these models to quantify the hot-nuclear-matter suppression.

PACS numbers: 25.75.Dw

Heavy quarkonia have long been proposed as a sensitive probe of the color screening length and deconfinement in the quark-gluon plasma [1]. The picture that was originally proposed is complicated by other competing effects that modify quarkonia production and survival in cold and hot nuclear matter. The large suppression of J/ψ in Pb+Pb collisions at $\sqrt{s_{NN}} = 17.2$ GeV measured by the NA50 experiment indicated suppression beyond that projected from cold nuclear matter effects and led to the initial conclusion that color screening was the dominant mechanism [2–4]. The expectation was that at the Relativistic Heavy Ion Collider (RHIC), where higher energy densities and temperatures are created, the J/ψ suppression would be stronger and turn on in even more peripheral collisions. However, measurements from the PHENIX experiment’s 2004 data set in Au+Au collisions at $\sqrt{s_{NN}} = 200$ GeV revealed that the centrality-dependent nuclear modification factor R_{AA} at midrapidity was the same within statistical and systematic uncertainties as the NA50 result [5–7]. In addition, for more central collisions ($N_{\text{part}} \gtrsim 100$) the suppression was measured to be larger at forward rapidity ($1.2 < |y| < 2.2$) compared with midrapidity [5]. This is opposite to the expectation that the suppression should be less at forward rapidity, where the energy density is lower.

The initial estimates of cold nuclear matter (CNM) effects in the NA50 Pb+Pb data were based on $p+A$ measurements [8] at higher collision energies. More recently, measurements of J/ψ production in $p+A$ collisions at $\sqrt{s_{NN}} = 17.2$ GeV made by NA60 have shown that CNM effects are stronger than the initial estimates,

due to a substantially larger J/ψ effective breakup cross section [9]. This resulted in a reduction of the estimated suppression due to possible hot nuclear matter effects from $\sim 50\%$ to $\sim 25\%$, relative to cold nuclear matter effects. Based on a systematic study of the energy dependence [10] the breakup cross section is expected to be much smaller at the higher RHIC energies, leading to smaller overall CNM effects. Thus it now seems that at RHIC the suppression beyond cold nuclear matter effects at midrapidity could be higher compared to the NA50 results, as one would expect due to the higher energy density. However, the question of why the observed suppression at RHIC is stronger at forward rapidity than at midrapidity remains less understood.

Since that first PHENIX measurement, many alternative explanations have been proposed which now require rigorous confrontation with the full set of experimental measurements. In this paper, we detail the measurement of forward rapidity J/ψ yields and modifications in Au+Au collisions at $\sqrt{s_{NN}} = 200$ GeV from data taken by the PHENIX experiment in 2007. The data set is more than three times larger than the earlier published 2004 data set. In addition, significant improvements in our understanding of the detector performance and signal extraction have led to a reduction in systematic uncertainties. We present details of this new analysis as well as comparisons with theoretical calculations that have attempted to reconcile the earlier data in terms of competing physics mechanisms.

I. DATA ANALYSIS

The PHENIX experiment is described in detail in [11]. For the forward rapidity J/ψ data analysis presented here, the PHENIX experiment utilizes one global detector, the beam-beam counter (BBC), for event central-

*Deceased

†PHENIX Spokesperson: jacak@skipper.physics.sunysb.edu

ity characterization and z -vertex determination, and two muon spectrometers (North and South) for measuring the J/ψ via the dimuon decay channel. The BBC is described in detail in [12]. It comprises two arrays of 64 quartz Čerenkov counters that measure charged particles within the pseudorapidity range ($3.0 < |\eta| < 3.9$). The BBC is also used as the primary Level-1 trigger for Au+Au minimum bias events. The two muon spectrometers are described in detail in [13], and comprise an initial hadronic absorber followed by three sets of cathode strip chambers in a magnetic field, referred to as the Muon Tracker (MuTR). Finally, there are five planes of active Iarocci tubes interleaved with additional steel absorber plates, referred to as the Muon Identifier (MuID). The muon spectrometers measure J/ψ s over the rapidity range $1.2 < |y| < 2.2$.

The PHENIX data acquisition system is capable of recording minimum bias Au+Au collisions at high rates (> 5 kHz) with a data archival rate in excess of 600 MB/s. During the 2007 Au+Au run at $\sqrt{s_{NN}} = 200$ GeV, the experiment recorded 82% of all collisions where the minimum bias level-1 trigger fired. Therefore no additional muon-specific trigger was necessary. After data quality cuts to remove runs where there were significant detector performance variations, we analyzed 3.6×10^9 minimum bias Au+Au events. The BBC Level-2 trigger used as the minimum bias trigger for Au+Au events required at least two hits in each of the BBC arrays and a fast-reconstructed z -vertex within ± 30 cm of the nominal center of the detector. An additional selection for our minimum bias definition in offline reconstruction includes a requirement of at least one neutron hit in each of our Zero Degree Calorimeters (ZDCs). This removes a 1-2% background event contamination in the peripheral event sample. The minimum bias definition corresponds to $92\% \pm 3\%$ of the inelastic Au+Au cross section [5]. We further categorize the events in terms of centrality classes by comparing the combined North and South BBC charge to a negative binomial distribution for the number of produced particles within the BBC acceptance combined with a Glauber model of the collision [14]. For each centrality category, the mean number of participating nucleons (N_{part}), binary collisions (N_{coll}), and impact parameter (b), and their associated systematic uncertainties are shown in Table I.

From this minimum bias data sample, we reconstruct muon candidates by finding tracks that penetrate through all layers of the MuID, then matching to tracks in the MuTR. The requirement of the track penetrating the full absorber material through the MuID significantly reduces the hadron contribution. However, there is a small probability of order $\sim 1/1000$ for a charged hadron to penetrate the material without suffering a hadronic interaction. This is referred to as a punch-through hadron. Additionally, the current muon spectrometer cannot reject most muons that originate from charged pions and kaons which decay before the absorber in front of the MuTR. Pairs of muon candidate tracks are selected and

TABLE I: Mean N_{part} , N_{coll} , and impact parameter values and systematic uncertainties in each centrality category.

Centrality (%)	$\langle N_{\text{part}} \rangle$	$\langle N_{\text{coll}} \rangle$	$\langle b \rangle$ (fm)
0–5	350.8 \pm 3.1	1067.0 \pm 107.7	2.3 \pm 0.1
5–10	301.7 \pm 4.7	857.8 \pm 85.5	3.9 \pm 0.1
10–15	255.7 \pm 5.4	680.2 \pm 67.3	5.2 \pm 0.2
15–20	216.4 \pm 5.6	538.7 \pm 52.4	6.1 \pm 0.2
20–25	182.4 \pm 5.7	424.4 \pm 40.4	7.0 \pm 0.3
25–30	152.7 \pm 5.9	330.9 \pm 32.7	7.7 \pm 0.3
30–35	126.8 \pm 5.9	254.7 \pm 25.8	8.4 \pm 0.3
35–40	104.2 \pm 5.8	193.1 \pm 20.7	9.0 \pm 0.3
40–45	84.6 \pm 5.6	143.9 \pm 16.5	9.6 \pm 0.4
45–50	67.7 \pm 5.4	105.4 \pm 13.5	10.2 \pm 0.4
50–55	53.2 \pm 5.0	75.2 \pm 10.5	10.7 \pm 0.4
55–60	41.0 \pm 4.5	52.5 \pm 8.2	11.2 \pm 0.4
60–65	30.8 \pm 3.9	35.7 \pm 6.1	11.7 \pm 0.5
65–70	22.6 \pm 3.4	23.8 \pm 4.7	12.2 \pm 0.5
70–75	16.1 \pm 2.8	15.4 \pm 3.3	12.6 \pm 0.5
75–80	11.2 \pm 2.2	9.7 \pm 2.3	13.1 \pm 0.5
80–92	5.6 \pm 0.8	4.2 \pm 0.8	13.9 \pm 0.5
0–20	280.5 \pm 4.6	783.2 \pm 77.5	4.4 \pm 0.2
20–40	141.5 \pm 5.8	300.8 \pm 29.6	8.0 \pm 0.3
40–60	61.6 \pm 5.1	94.2 \pm 12.0	10.4 \pm 0.4
60–92	14.4 \pm 2.1	14.5 \pm 2.8	13.0 \pm 0.5

a combined fit is performed with the collision z -vertex from the BBC. We apply various cuts to enhance the sample of good muon track pairs, including cuts on the individual track χ^2 values, the matching between position and direction vectors of the MuID track and the MuTR track projected to the front of the MuID, and finally the track pair and BBC z -vertex combined fit χ^2_{vtx} .

We then calculate the invariant mass of all muon candidate unlike charged sign pairs in various bins in rapidity, p_T , and centrality. Due to the high particle multiplicity in Au+Au events, there is a significant background under the J/ψ peak. In the 0-5% most central Au+Au collisions, within the mass window around the J/ψ ($2.6 < M$ [GeV/ c^2] < 3.6) the signal to background is of order 2.9% in the South muon spectrometer and 0.7% in the North muon spectrometer (which has a different geometric acceptance and significantly higher occupancy). The background comprises two components. First, there is the combinatorial background from uncorrelated track pairs. Second, there is a correlated background from physical sources including open charm pair decays (e.g. $D^0 + \bar{D}^0 \rightarrow (K^- \mu^+ \nu_\mu) + (K^+ \mu^- \bar{\nu}_\mu)$), open beauty pair decays, and Drell-Yan. The combinatorial background is estimated and subtracted by using event mixing to recreate the background from uncorrelated pairs. Pairs are created from different Au+Au events

within the same category in Au+Au centrality and BBC collision z-vertex. The mixed-event invariant mass distributions are calculated for unlike-sign and like-sign pairs. We treat the real event like-sign pairs as being purely from combinatorial background, since the contribution of the above-mentioned correlated physical background is negligible relative to the combinatorial background. Thus, we determine the mixed event normalization for the unlike-sign case by calculating the normalization factor between the mixed event and real event like-sign counts. We have confirmed that the mixed event and real event like-sign invariant mass distributions match over the full mass range used in the analysis.

The total J/ψ counts recorded in all Au+Au collisions are ~ 9100 and ~ 4900 in the south and north muon spectrometers, respectively. Two example unlike-sign invariant mass distributions before (upper panel) and after (lower panel) mixed-event combinatorial background subtraction are shown in Fig. 1. The number of measured J/ψ is derived from the subtracted spectra by fitting to the data the line shape of the J/ψ , as determined in $p+p$ collisions [15], and an exponential for the remaining correlated physical background. Note that in the higher $p_T > 2$ GeV/ c bins, there is some small acceptance for the ρ , ω and ϕ and thus these additional components are included in the fit. At low p_T , the acceptance goes to zero for lower invariant mass due to the minimum required momentum for each muon to penetrate the MuID and the angular acceptance of the spectrometer. This is accounted for by folding the fit function with an acceptance function that is calculated from Monte Carlo simulation and goes to zero at small invariant mass, as expected. We perform a set of fits where we vary the invariant mass range, the line shape of the J/ψ , and the normalization of the mixed-event sample by $\pm 2\%$ to determine the mean extracted J/ψ signal and systematic uncertainty from the RMS of the different results. Note that any bin where the extracted signal is of less than one standard deviation significance (including statistical and systematic uncertainties) is quoted as a 90% confidence level upper limit (CLUL) based on Poisson statistics.

We also estimated the combinatorial background using the like-sign method, i.e. $N_{+-}^{comb} = 2\sqrt{N_{++} \times N_{--}}$. In this case there is no event mixing, the background is estimated purely from same-event like-sign pairs (instead of mixed-event pairs). The two methods agree over most of the centrality range; however, for the more central events the like-sign method results in somewhat lower extracted counts ($\sim 10\%$). We take the average of the two signal extraction methods and assign an additional systematic uncertainty due to the difference, although for peripheral bins it is a negligible difference.

We then calculate the J/ψ invariant yield for each centrality bin and also in bins in p_T by the following equation:

$$B_{\mu\mu} \frac{d^3 N}{dp_T^2 dy} = \frac{1}{2\pi p_T \Delta p_T \Delta y} \frac{N_{J/\psi}}{A\epsilon N_{EVT}} \quad (1)$$

where $B_{\mu\mu}$ is the branching fraction of J/ψ to muons, $N_{J/\psi}$ is the number of measured J/ψ , N_{EVT} is the number of events in the relevant Au+Au centrality category, $A\epsilon$ is the detector geometric acceptance and efficiency, and Δp_T and Δy are the bin width in p_T and y . For the p_T -integrated bins, we similarly calculate $B_{\mu\mu} dN/dy = N_{J/\psi}/(A\epsilon N_{EVT} \Delta y)$.

We calculate $A\epsilon$ to correct for the geometric acceptance of the detector and the inefficiencies of the MuTR and MuID, the track finding algorithm, and occupancy-related effects in the Au+Au environment. This is done by propagating PYTHIA-generated J/ψ through the PHENIX GEANT-3 [16] detector simulation, and embedding the resulting hits in real Au+Au events. The events are then reconstructed using the identical analysis as for real data, and the ratio is taken between reconstructed and embedded J/ψ . The resulting $A\epsilon$ as a function of centrality is shown in Fig. 2 for both the North and South Muon Arms. The effect of the detector occupancy can be seen for more central events, as well as the higher occupancy and resulting lower efficiency in the North Arm.

The acceptance and efficiency as a function of p_T is relatively flat, with a modest 20% decrease from $p_T = 0$ to $p_T \sim 2.5$ GeV/ c^2 , then proceeds to rise again. The behavior is essentially the same across centralities, with the only difference being the absolute scale of $A\epsilon$.

We calculate the invariant yields separately from the two muon spectrometers, and then combine the values for the final results. We take the weighted average based on the statistical uncertainties and those systematic uncertainties which are uncorrelated between the two measurements. The final averaged result is assigned the uncorrelated (reduced by the averaging) and correlated systematic uncertainties. In addition, it was found that the invariant yields from the two spectrometers disagree beyond their independent uncertainties, and a 5% systematic was added to account for the difference.

II. RESULTS

The final J/ψ invariant yields in 5%-wide centrality bins (integrated over all p_T) are listed in Table II, and as a function of p_T in broader 20%-wide centrality bins in Table III.

The nuclear modification factor R_{AA} compares J/ψ production in A + A with binary collision-scaled $p + p$ reactions, and is calculated as:

$$R_{AA} = \frac{1}{\langle N_{coll} \rangle} \frac{dN^{A+A}/dy}{dN^{p+p}/dy} \quad (2)$$

where $\langle N_{coll} \rangle$ is the mean number of binary collisions in the centrality category of interest. The $p + p$ results are from the combined analysis of data taken in 2006 and 2008 as published in [17]. The resulting R_{AA} as a function of N_{part} for J/ψ from Au+Au collisions is shown as red circles in Fig. 3.

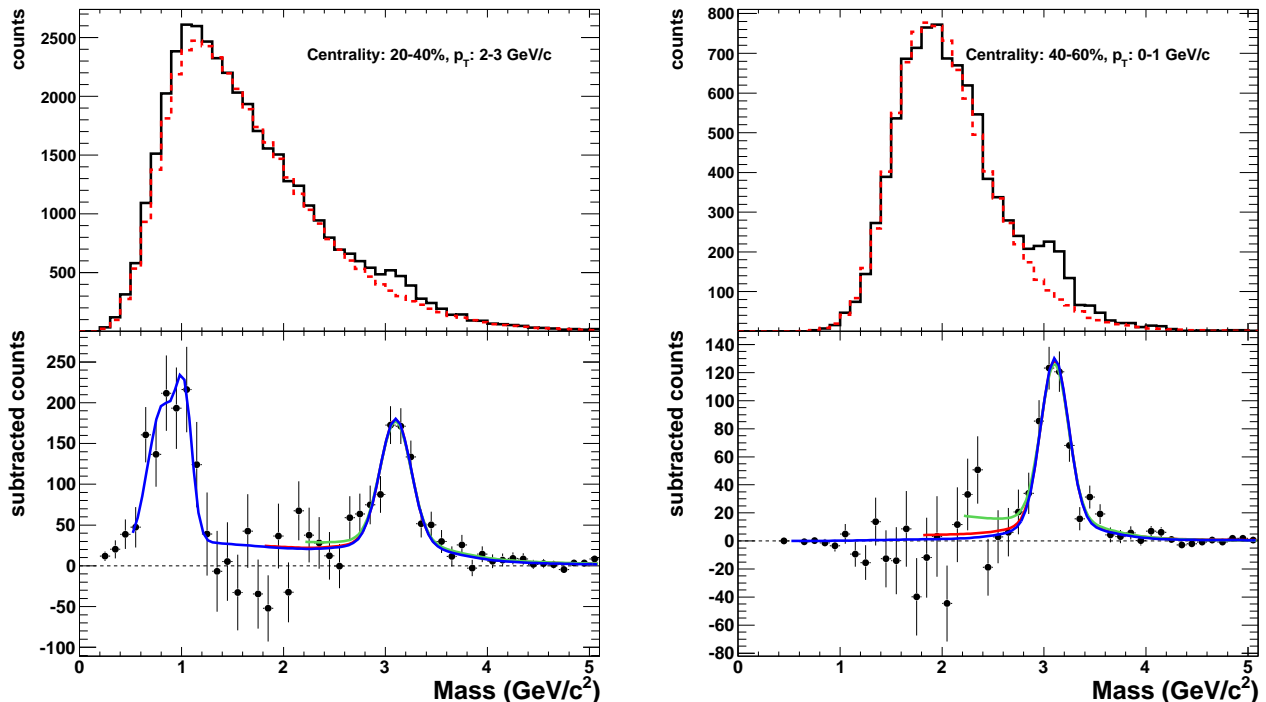


FIG. 1: (Color online) Top: muon spectrometer unlike-sign invariant mass distributions from same-event pairs (black, solid) and mixed-event pairs (red, dashed). Two example centralities and transverse momentum ranges are shown. Bottom: Corresponding unlike-sign invariant mass distributions after mixed-event combinatorial-background subtraction. Colored curves represent three different mass ranges for the signal extraction fit.

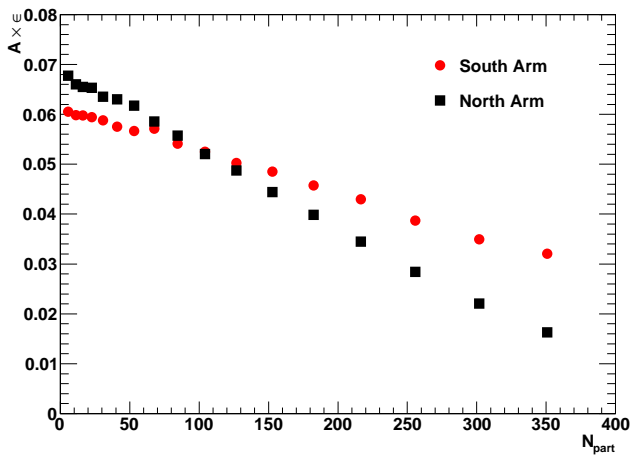


FIG. 2: (Color online) Acceptance \times efficiency as a function of centrality for the North and South Arms.

The systematic uncertainties are divided into three categories: type A are the point-to-point uncorrelated systematics, type B are correlated (or anti-correlated) point-to-point, and type C are 100% correlated (i.e. a common multiplicative factor) between all of the points. The error bars in Figs. 3–10 represent the statistical and type A uncertainties added in quadrature, the boxes represent the type B uncertainties, while the type C systematics are

included as text in the labels. The type A uncertainties are the RMS of the various mass fits as described above. The type B uncertainties on R_{AA} are comprised

TABLE II: J/ψ invariant yields $B_{\mu\mu}dN/dy$ at forward rapidity ($1.2 < |y| < 2.2$) vs. Au+Au collision centrality. The type C (global) uncertainty for all points is 10.7%.

Centrality (%)	$B_{\mu\mu}dN/dy$	\pm stat	\pm type A	+type B	-type B	scale
				(GeV/c ⁻²)		
0–5	1.25	0.27	0.11	0.24	0.12	$\times 10^{-4}$
5–10	9.12	2.46	0.13	1.15	0.81	$\times 10^{-5}$
10–15	9.37	1.66	0.71	1.01	0.95	$\times 10^{-5}$
15–20	9.16	1.24	0.48	1.08	1.08	$\times 10^{-5}$
20–25	7.11	0.98	0.29	0.64	0.64	$\times 10^{-5}$
25–30	7.85	0.74	0.29	0.64	0.64	$\times 10^{-5}$
30–35	6.14	0.57	0.28	0.49	0.49	$\times 10^{-5}$
35–40	5.43	0.45	0.14	0.52	0.52	$\times 10^{-5}$
40–45	5.07	0.37	0.15	0.39	0.39	$\times 10^{-5}$
45–50	3.49	0.28	0.07	0.30	0.30	$\times 10^{-5}$
50–55	2.76	0.21	0.07	0.21	0.21	$\times 10^{-5}$
55–60	2.85	0.17	0.04	0.21	0.21	$\times 10^{-5}$
60–65	1.64	0.14	0.03	0.12	0.12	$\times 10^{-5}$
65–70	1.17	0.10	0.01	0.09	0.09	$\times 10^{-5}$
70–75	9.49	0.85	0.11	0.73	0.73	$\times 10^{-6}$
75–80	6.79	0.69	0.14	0.51	0.51	$\times 10^{-6}$
80–92	3.43	0.29	0.04	0.26	0.26	$\times 10^{-6}$

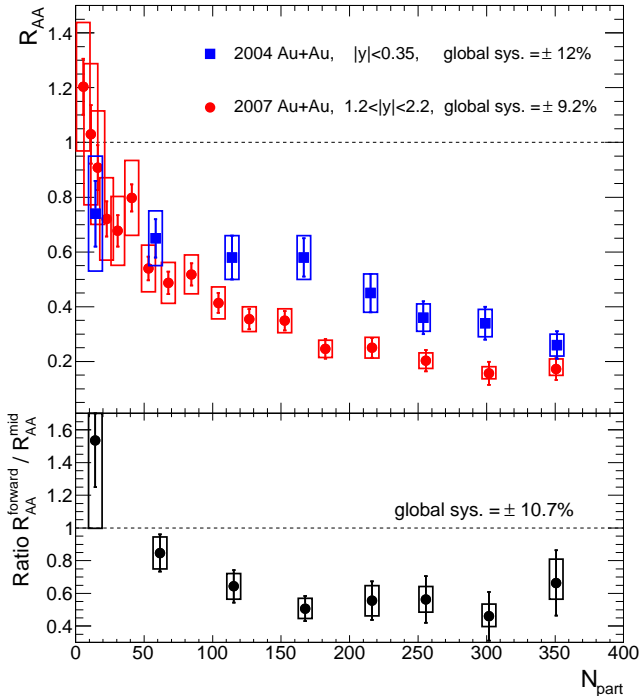


FIG. 3: (Color online) J/ψ R_{AA} as a function of N_{part} . Error bars represent the statistical and uncorrelated systematic uncertainties, while the boxes represent the point-to-point correlated systematics. The global scale systematic uncertainties are quoted as text. The lower panel contains the ratio of forward rapidity to midrapidity for the points in the upper panel.

of many sources, dominated by uncertainties in $\langle N_{coll} \rangle$, uncertainties in the matching of Monte Carlo and real detector performance, and differences in signal extraction methods. The type C uncertainties are dominated by the normalization in the $p + p$ invariant cross section measurement. Important systematics on the invariant yields are listed in Table IV.

For comparison, in Fig. 3 we show our previously-published midrapidity J/ψ R_{AA} values from data taken in 2004 [5]. The midrapidity measurement was made in the PHENIX central spectrometers via the J/ψ dielectron decay. There is no PHENIX updated measurement at midrapidity from the 2007 data set due to significantly increased conversion backgrounds from this engineering run of the PHENIX Hadron Blind Detector [18]. The ratio of the new forward rapidity data to the previously-published midrapidity data, shown in the lower panel of Fig. 3, is in agreement with the previous result [5], where the latter led to speculation as to what mechanism could cause a narrower rapidity distribution in Au+Au than $p + p$ collisions.

We also calculate R_{AA} as a function of p_T , again using the published 2006 and 2008 $p + p$ data [17]. Shown in Fig. 4 are the new results at forward rapidity along with the previously-published 2004 midrapidity results [5]. In

TABLE III: J/ψ invariant yields $B_{\mu\mu} \frac{d^3N}{dp_T^2 dy}$ at forward rapidity ($1.2 < |y| < 2.2$) vs. p_T in four bins of Au+Au collision centrality. The type C (global) uncertainties are 10%, 10%, 13%, and 19% for 0-20%, 20-40%, 40-60%, and 60-92% centrality, respectively. Bins in which the J/ψ yield was less than the combined statistical and systematic uncertainties are calculated as 90% Confidence Level Upper Limits (CLUL).

Centrality (%)	p_T (GeV/c)	$B_{\mu\mu} \frac{d^3N}{dp_T^2 dy}$	stat	type A	+B	-B	scale
0-20	0-1	9.36	1.41	0.74	1.01	1.01	$\times 10^{-6}$
	1-2	4.46	0.66	0.23	0.40	0.40	$\times 10^{-6}$
	2-3	1.37	0.29	0.08	0.17	0.17	$\times 10^{-6}$
	3-4	2.99	1.12	0.09	0.27	0.27	$\times 10^{-7}$
	4-5	2.05	0.43	0.14	0.18	0.18	$\times 10^{-7}$
	5-6						90% CLUL = 3.27×10^{-8}
	6-7						90% CLUL = 2.00×10^{-8}
20-40	0-1	5.08	0.54	0.18	0.67	0.67	$\times 10^{-6}$
	1-2	2.78	0.22	0.09	0.26	0.26	$\times 10^{-6}$
	2-3	1.11	0.10	0.02	0.09	0.09	$\times 10^{-6}$
	3-4	2.76	0.34	0.11	0.25	0.25	$\times 10^{-7}$
	4-5	7.47	1.37	0.31	1.35	1.35	$\times 10^{-8}$
	5-6	2.68	0.61	0.08	0.31	0.31	$\times 10^{-8}$
	6-7						90% CLUL = 7.15×10^{-9}
40-60	0-1	3.19	0.21	0.06	0.26	0.26	$\times 10^{-6}$
	1-2	1.49	0.09	0.03	0.12	0.12	$\times 10^{-6}$
	2-3	4.80	0.38	0.11	0.39	0.39	$\times 10^{-7}$
	3-4	1.27	0.13	0.02	0.11	0.11	$\times 10^{-7}$
	4-5	3.86	0.49	0.02	0.41	0.41	$\times 10^{-8}$
	5-6	7.51	1.69	0.05	2.04	2.04	$\times 10^{-9}$
	6-7						90% CLUL = 2.82×10^{-9}
60-92	0-1	9.05	0.57	0.07	0.73	0.73	$\times 10^{-7}$
	1-2	3.40	0.22	0.04	0.27	0.27	$\times 10^{-7}$
	2-3	9.19	0.91	0.16	0.75	0.75	$\times 10^{-8}$
	3-4	2.21	0.35	0.04	0.20	0.20	$\times 10^{-8}$
	4-5	8.13	1.39	0.01	0.70	0.70	$\times 10^{-9}$
	5-6	2.31	0.54	0.00	0.40	0.40	$\times 10^{-9}$
	6-7						90% CLUL = 7.69×10^{-10}

TABLE IV: Systematic uncertainties on dN/dy for central and peripheral centrality categories.

Source	Central	Peripheral	Type
Signal extraction	9.8%	1.3%	A
Acceptance	3.4%	2.2%	B
Input y , p_T distributions	4%	4%	B
Difference between mixed event/ like-sign background estimates	1.5%	0.6%	B
North/south arm agreement	5%	5%	B
MuID efficiency	3.6%	2.8%	B

some centrality bins for $p_T > 5$ GeV/c, we have no significant J/ψ signal in Au+Au and thus can only quote a

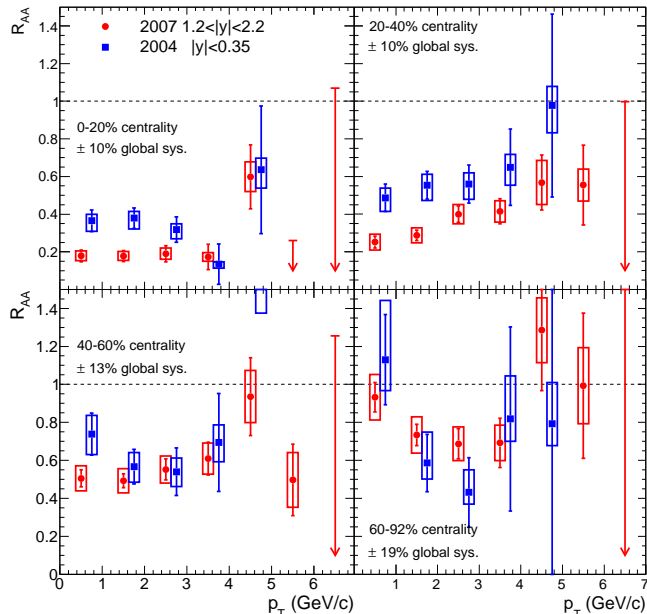


FIG. 4: (Color online) J/ψ R_{AA} as a function of p_T in four centrality bins. Error bars represent the statistical and uncorrelated systematic uncertainties, while the boxes represent the point-to-point correlated systematic uncertainties. The global scale systematic uncertainties are quoted as text.

90% confidence level upper limit on R_{AA} .

As there has been much recent interest in whether the R_{AA} as a function of p_T rises or falls, we have performed a simple linear fit to the R_{AA} at forward rapidity over the full p_T range and obtain the following slope (m) values: $m = +0.011 \pm 0.018$ c/GeV (0-20% central), $m = +0.065 \pm 0.023$ c/GeV (20-40% central), $m = +0.034 \pm 0.033$ c/GeV (40-60% central), and $m = -0.037 \pm 0.053$ c/GeV (60-92% central). The quoted slope uncertainties are the quadrature sum of the statistical and systematic uncertainties. Thus, only the 20-40% centrality indicates a statistically significant increase in R_{AA} with p_T .

III. MODEL COMPARISONS

As previously mentioned, various theoretical models have been proposed to reconcile the J/ψ suppression pattern previously published [5]. Here we compare our measurements with three calculations for the centrality and rapidity dependence of the suppression. The first deals entirely with initial-state effects, while the other two incorporate strong final-state effects. Then we compare our measurements with a simple cold nuclear matter effect calculation extrapolated to Au+Au collisions. Finally, we compare to a model calculation for the p_T dependence of R_{AA} at forward rapidity.

In addition to the models discussed here, there are many more models that only have a midrapidity predic-

tion for J/ψ production. Because this paper is focused on forward rapidity J/ψ production, we have not included comparisons to those models.

A. Gluon Saturation Model

In the first model by Kharzeev et. al [19], it is assumed that the nuclear wave functions in very high-energy nuclear collisions can be described by the Color Glass Condensate (CGC). The primary effect is the suppression of J/ψ production and narrowing of the rapidity distribution due to saturation of the gluon fields in heavy ion collisions relative to $p + p$ collisions. In addition, the production mechanism is modified from $p + p$ such that the multigluon exchange diagrams are enhanced. It should be noted that this model does not include any hot medium effects, but does have a free parameter for the overall normalization factor for the Au+Au production, which is fixed to match the midrapidity central collision J/ψ suppression. Thus, the suppression trend with centrality and the relative suppression between mid and forward rapidity are predicted, but not the overall level of suppression.

The resulting R_{AA} values calculated using this model are shown in Fig. 5. This model provides a reasonable description of the data and in particular matches the observed larger suppression at forward rapidity than mid rapidity in central events ($R_{AA}^{\text{forward}}/R_{AA}^{\text{mid}} \sim 0.5$). It is notable that this ratio is essentially independent of centrality in their calculation, whereas the experimental data shows the relative suppression approaching one in the most peripheral events. Additionally, the calculation at midrapidity actually indicates a significant enhancement (i.e. $R_{AA} > 1$) for peripheral events with $N_{\text{part}} < 50$. This enhancement is related to a coherence effect of double gluon exchange. However, the coherence predicts an enhancement in $d+\text{Au}$ collisions and $R_{d\text{Au}}$ at midrapidity, and no such enhancement is seen in the experimental data [17].

Recently, the appropriate normalization factor for the above CGC calculation has been calculated [20, 21]. Replacing the normalization factor previously applied to match the theory to the magnitude of the observed midrapidity suppression, results in a predicted CGC suppression approximately a factor of two smaller than in the $\sqrt{s_{NN}}$ data. This result suggests the importance of additional hot nuclear matter effects.

B. Comover Interaction Model

The second calculation comes from the Comover Interaction Model (CIM) [22, 23]. This calculation uses a rate equation that accounts for J/ψ breakup due to interactions with a dense co-moving final-state medium. Additionally, the contribution from interactions with the outgoing nuclei is included. No assumption is made about

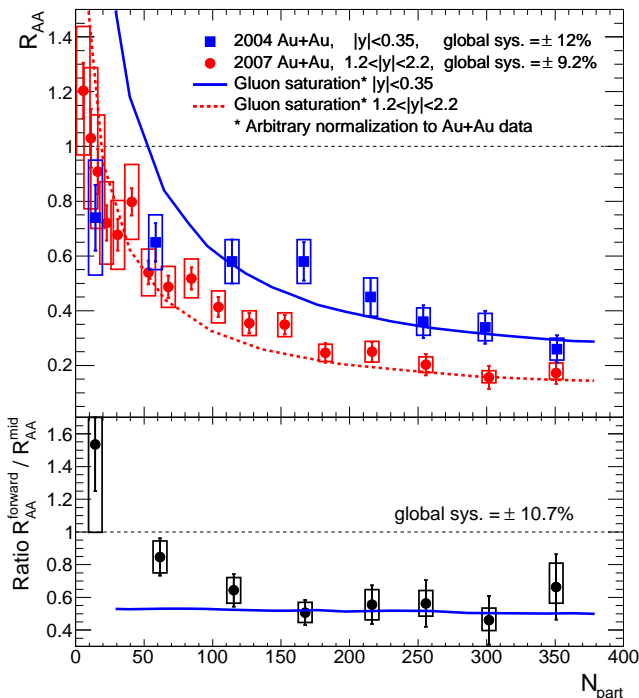


FIG. 5: (Color online) J/ψ R_{AA} as a function of N_{part} . Model calculation from [19]. Lower panel is the ratio of forward to midrapidity points and curves from the upper panel.

the nature of the co-moving medium, i.e. whether it is partonic or hadronic, only that it can be represented by a comover density and comover- J/ψ cross section σ_{co} , for which a value of 0.65 mb was found to match the NA50 data and then used for the projection to Au+Au at RHIC. The separate nuclear breakup cross section was taken to be $\sigma_{br} = 4.5$ mb. This value was taken from measurements in $p+A$ collisions at $\sqrt{s_{NN}} = 27.4/29.1$ GeV at the CERN-SPS. Under the assumption that σ_{br} is energy-independent, the value from those measurements was used until recently as the cold nuclear matter reference for heavy ion collisions at $\sqrt{s_{NN}} = 17.2$ GeV [2], as well as in [22] as the reference for $\sqrt{s_{NN}} = 200$ GeV at RHIC.

However, the effective breakup cross section has now been shown to decrease significantly with collision energy [10]. In fact, a recent measurement in $p+A$ collisions at $\sqrt{s_{NN}} = 17.2$ GeV [9] yielded a value of $\sigma_{br} = 7.6 \pm 0.7 \pm 0.6$ mb with no anti-shadowing correction, and $\sigma_{br} = 9.3 \pm 0.7 \pm 0.7$ mb with anti-shadowing corrected for. The value measured in $d+Au$ collisions at RHIC [15] is $2.8^{+1.7}_{-1.4}$ mb (after shadowing is accounted for using EKS98 nuclear PDFs), somewhat smaller than the 4.5 mb used in [22]. The calculation, shown in Fig. 6 as the black, dot-dot-dashed curve, significantly overestimated the suppression measured at midrapidity for Au+Au collisions at $\sqrt{s_{NN}} = 200$ GeV [5, 7]. The suppression is stronger than the SPS case mainly due to the larger comover density calculated for RHIC.

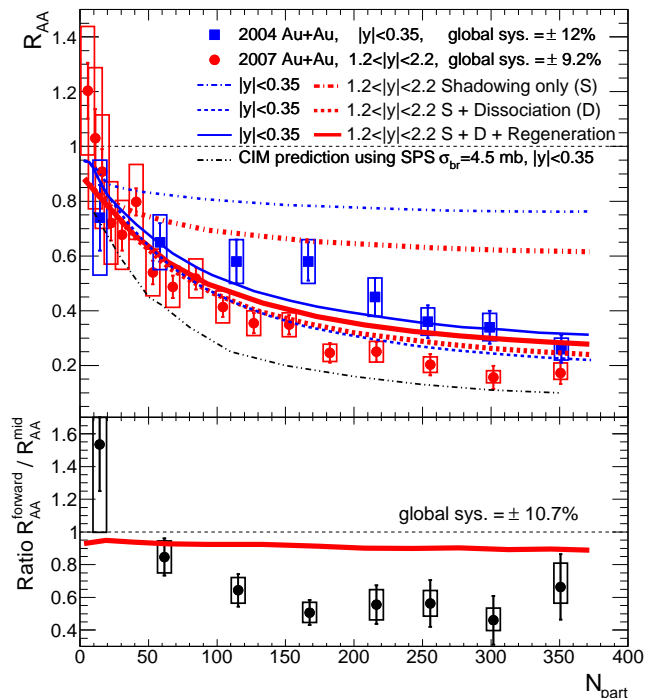


FIG. 6: (Color online) J/ψ R_{AA} as a function of N_{part} . Curves are calculations within the Co-mover Interaction Model (CIM). The black dot-dot-dashed curve is the older CIM calculation [22] predicted from SPS data. The remaining curves are from [23], where the dot-dashed curve is from shadowing alone, the dashed line also includes dissociation in the co-moving medium, and the solid line is the total effect after including J/ψ s from regeneration. The thin blue curves are calculated for midrapidity, while the thick red are for forward rapidity. The lower panel contains the ratio of forward rapidity to midrapidity for all points and curves in the upper panel where both are calculated.

An updated calculation [23] was then released that replaced the constant nuclear breakup cross section with a Bjorken- x -dependent function that goes to $\sigma_{br} = 0$ mb at $y = 0$, while the same $\sigma_{co} = 0.65$ mb was used for the comover interactions as before. Additionally, a J/ψ regeneration component was added that is normalized to the ratio of open charm production squared to J/ψ production in $p+p$ collisions. These new results are included in Fig. 6. The suppression from initial-state effects alone is much weaker at midrapidity than the previous calculation, due to both the change in the nuclear absorption, as well as an updated parametrization of shadowing effects.

The CNM effects (i.e. shadowing and nuclear absorption) are much stronger at forward rapidity than midrapidity, due in part to the assertion that nuclear absorption is negligible at midrapidity. On the other hand, the effects of comover dissociation and regeneration are stronger at midrapidity. The combination of these three effects leads to predictions which are overall very similar at forward and midrapidity (as seen in the lower panel).

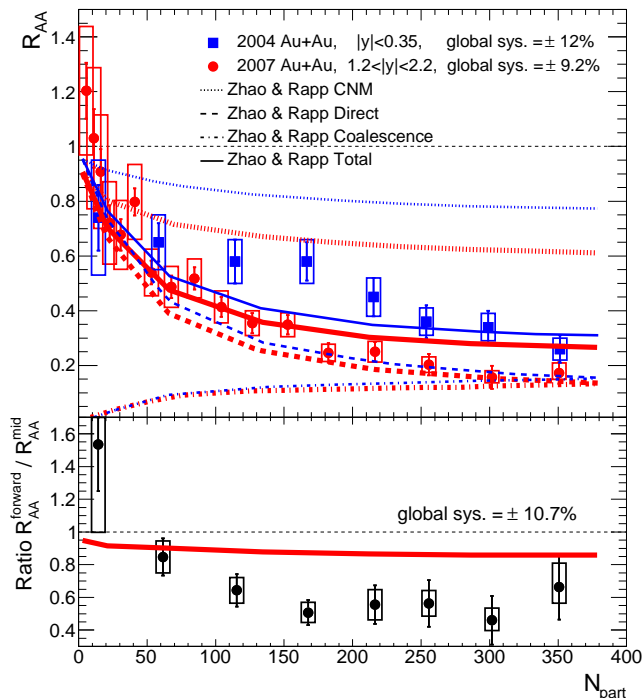


FIG. 7: (Color online) J/ψ R_{AA} as a function of N_{part} . Model calculations by Zhao and Rapp from [24, 25] are included for both rapidity bins, incorporating cold and hot nuclear matter suppression as well as coalescence of $c\bar{c}$ pairs. The various line styles represent the different contributions to the total as laid out in the legend, while the two thicknesses represent the two rapidity ranges (thin blue is midrapidity and thick red is forward rapidity). The lower panel contains the ratio of forward rapidity to midrapidity for all points and curves in the upper panel.

C. QGP/Hadron Gas Model

The third model we compare with is from Zhao and Rapp [24, 25], which incorporates both a quark-gluon plasma (QGP) phase and a hadronic gas (HG) phase. In this calculation, they include two different models for cold nuclear matter effects. In the first case, nuclear absorption is calculated in the usual Glauber formalism, shadowing plus anti-shadowing are assumed to roughly cancel, such that the overall shadowing effects are encapsulated in the breakup cross section σ_{br} , and p_T broadening is included via Gaussian smearing. In the second case, the cold nuclear matter effects are treated as in [23], supplemented with the same p_T broadening model as the first case.

The thermal dissociation is modeled via a Boltzmann transport equation for both QGP and HG phases. The QGP is assumed to be an isentropically expanding cylindrical fireball. J/ψ -medium interactions are assumed to stop at a freeze-out temperature of 120 MeV. The final J/ψ p_T distribution is calculated by spatially integrating the final phase-space distribution. The regeneration

component assumes that the $c\bar{c}$ is thermally equilibrated with the medium when it coalesces into a J/ψ . Consequently, and the ψ p_T distribution is governed by a blastwave equation for the transverse flow velocity. The normalization of this component is performed by plugging the initial charm densities into a rate equation with both gain and loss terms, and solving at the freeze-out time.

The calculation results, using the second case for the cold nuclear matter effects, are shown in Fig. 7, along with the separate dissociation and regeneration components. Though the second cold nuclear matter case increases the suppression for more central events compared to the first scenario, the difference in the overall suppression between the two scenarios is small. The qualitative trends of the calculation agree with the experimental data; however, the calculated suppression is very similar between forward and midrapidity, which is in disagreement with the data.

It is noteworthy that the regeneration component is only slightly larger at midrapidity in this model than at forward rapidity. This is in contrast to other regeneration or recombination calculations that result in a significant narrowing of the J/ψ rapidity distribution in central Au+Au events (see for example [27, 28]). In simple calculations, the J/ψ recombination contribution scales as the square of the local charm density $((dN_{c\bar{c}}/dy)^2)$ and thus there is substantially less recombination at forward rapidity. This modeling also leads to predictions of significantly larger recombination enhancements at the LHC where charm production is much larger. However, in this calculation [25] with a full space-momentum distribution of charm pairs, the probability of a charm quark from one $c\bar{c}$ pair recombining with an anti-charm quark from another $c\bar{c}$ pair is suppressed because they are typically spatially separated which is then maintained through collective flow. Thus, their recombination is dominated by the case where a $c\bar{c}$ is produced as a pair that would normally not form a J/ψ , but due to scattering in the medium have a re-interaction and recombine. In this case, the regeneration contribution has a rapidity dependence similar to that of the directly produced J/ψ .

D. Shadowing/Nuclear Absorption/Initial-state Energy Loss Model

In addition to the above three models, we use a framework for calculating just the cold nuclear matter effects and extrapolating them to Au+Au collisions. We begin with the prescription in [26] for d +Au collisions, which combines effects of nuclear-modified parton distributions functions (nPDFs) using the EPS09 parameterization [29] with a rapidity-independent J/ψ -nucleon breakup cross section σ_{br} , along with the possibility of initial-state parton energy loss. We have extended these calculations to the Au+Au case using the identical code. First, we include the variations of the EPS09 nPDF sets

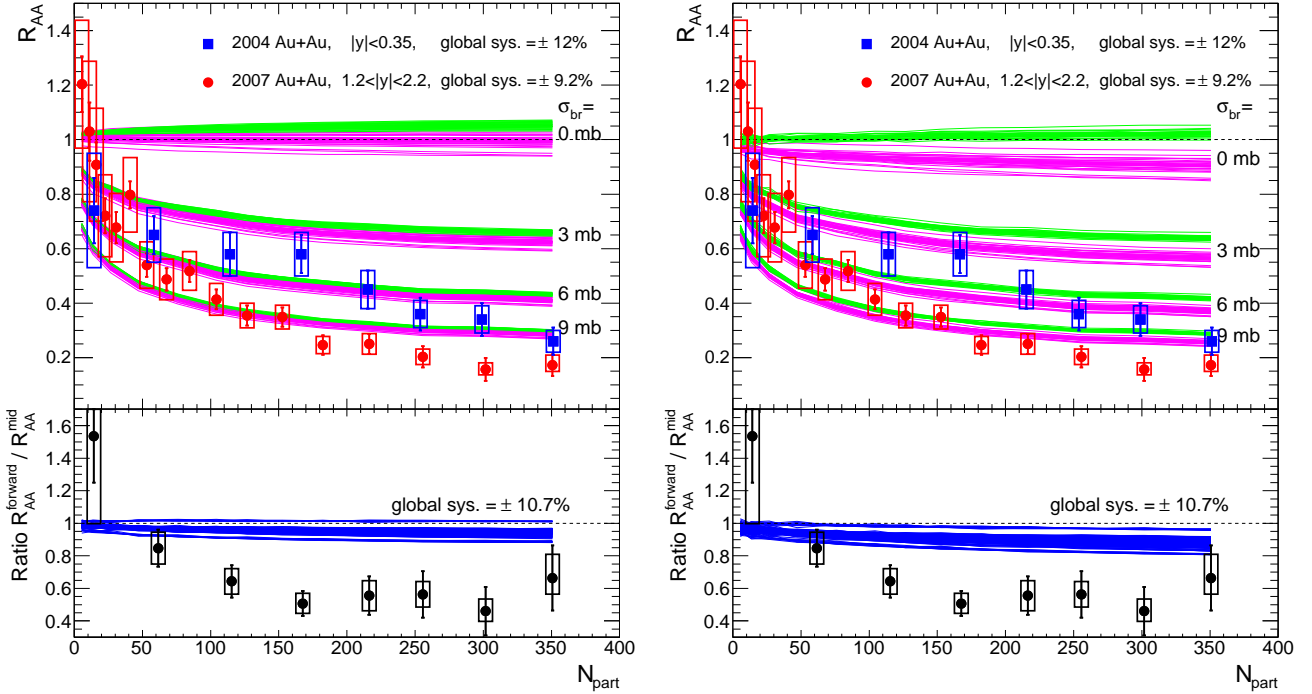


FIG. 8: (Color online) J/ψ R_{AA} as a function of N_{part} . Shown in the left panel is a comparison with a calculation including cold nuclear matter effects (nPDF and $\sigma_{breakup}$) following the prescription in [17, 26]. The green (magenta) lines (light gray) in B&W are the result at midrapidity (forward rapidity) for all 31 EPS09 nPDF variations and the labeled value for $\sigma_{breakup}$ for 0, 3, 6, and 9 mb. In the lower panel, one sees all 31 EPS09 variations times the various $\sigma_{breakup}$ values resulting in less than a 10% difference between forward and midrapidity modification. The right panel shows the same calculation, but now including initial state parton energy loss with a quadratic length dependence. The chosen strength of the energy loss is that which most closely matches the $d+Au$ data as detailed in paper [26]. The lower panels in both cases contain the ratios of forward rapidity to midrapidity for all points and curves in the upper panels.

and the breakup cross section σ_{br} . Shown in the left panel of Fig. 8, is the projected cold nuclear matter effect from these two contributions. The top green band shows the results for J/ψ at midrapidity from all 31 EPS09 nPDF variations with a $\sigma_{br} = 0$ mb. The lower green bands are in steps of $\sigma_{br} = 3, 6, 9$ mb. The magenta bands show results for J/ψ at forward rapidity. The centrality dependence is not reproduced for any value of σ_{br} at either rapidity, though a value of σ_{br} greater than 6 mb (9 mb) is required to approach the data at mid (forward) rapidity. In the lower panel we show all 31 EPS09 nPDFs times 4 σ_{br} values spanning the range $\sigma_{br} = 0-9$ mb for the ratio of the forward to midrapidity suppression. No combination of these two effects reproduces the modification in the rapidity shape for mid to central Au+Au collisions. One reason for the modest rapidity dependence is that at forward rapidity the J/ψ production results from one low- x gluon (in the nPDF shadowing regime) and one high- x gluon (in the nPDF anti-shadowing regime) and the two effects largely cancel.

As discussed in [26], one can attempt to improve the cold nuclear matter calculation agreement with the $d+Au$ data by including a parameterization of initial-state parton energy loss. In the right panel of Fig. 8, we again plot all 31 EPS09 nPDF parameterizations, 4 σ_{br} values and

the quadratic length dependent initial-state parton energy loss that best matched the $d+Au$ data. The initial-state parton energy loss has a minimal effect over this rapidity range, which is not unexpected since the effect only becomes significant in $d+Au$ for rapidity $y > 1.8$.

We note that the cold nuclear matter calculation does not give a full description of the $d+Au$ data, adding some uncertainty to its use in Au+Au collisions. Nevertheless, it is informative that the calculation clearly fails to simultaneously explain the Au+Au data at forward and midrapidity. We observe J/ψ suppression beyond that expected from the cold nuclear matter effects included in this calculation with the choice of a reasonable value of 3.0-3.5 mb for σ_{br} at RHIC.

E. p_T Dependence of the Suppression

Most of the above calculations do not include predictions for the J/ψ suppression as a function of transverse momentum. However, the calculation of Zhao and Rapp [25] provides nuclear modification factors at both mid- and forward rapidity as a function of p_T . Shown in Fig. 9 are the results compared with our experimental

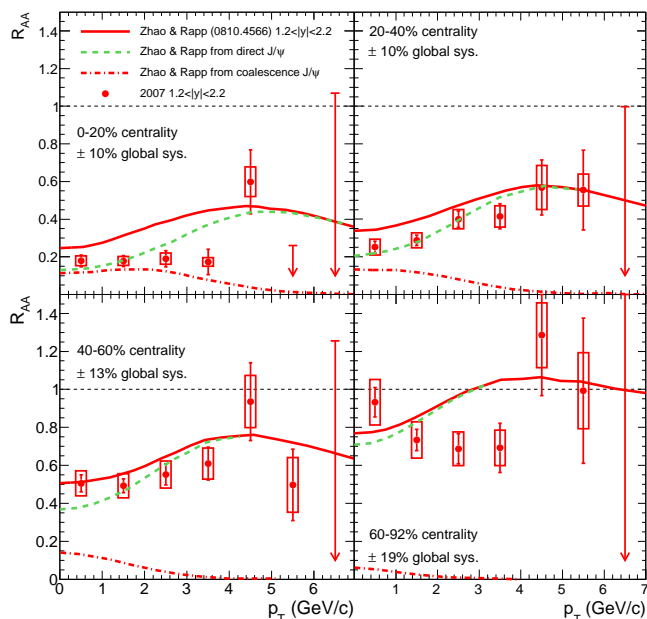


FIG. 9: (Color online) J/ψ R_{AA} as a function of p_T in four centrality bins. Model calculations by Zhao and Rapp from [24, 25] are included for the forward rapidity bin, incorporating cold and hot nuclear matter suppression as well as coalescence of $c\bar{c}$ pairs.

data. Their calculations indicate a moderate rise in R_{AA} versus p_T predominantly due to the Cronin effect [32]. In fact, in other recombination models the enhancement is limited to low p_T [27], and in this calculation the recombination contribution drops off beyond $p_T \gtrsim 3$ GeV/c. At low p_T in the most central bin, the suppression from this calculation is too weak by up to a factor of two.

More recently, Zhao and Rapp [30, 31] have modified this calculation to include feed-down from B -mesons and a reduced suppression at higher p_T due to the longer formation time of the preresonance state to the J/ψ from time dilation. These contributions serve to increase R_{AA} at higher p_T compared to the previous calculation, and are compared to the forward rapidity data in Fig. 10. The current lack of statistics in the data at $p_T > 5$ GeV/c precludes a confirmation of this effect.

It should also be noted that in the new calculation by Zhao and Rapp, cold nuclear matter effects are handled differently than in the earlier calculation. An effective absorption cross section of 3.5 (5.5) mb at $y = 0$ (1.7) is used to account for the combined effects of shadowing and breakup. These effective cross sections are obtained from comparison with recent PHENIX d +Au data. They argue that the larger effective breakup cross section at forward rapidity is most likely associated with shadowing effects, and so reflects a suppression of the number of charm pairs relative to midrapidity. Therefore, the additional effective absorption at forward rapidity is associated with a reduction in the open charm yield as well as the J/ψ yield, thus also reducing the J/ψ regeneration

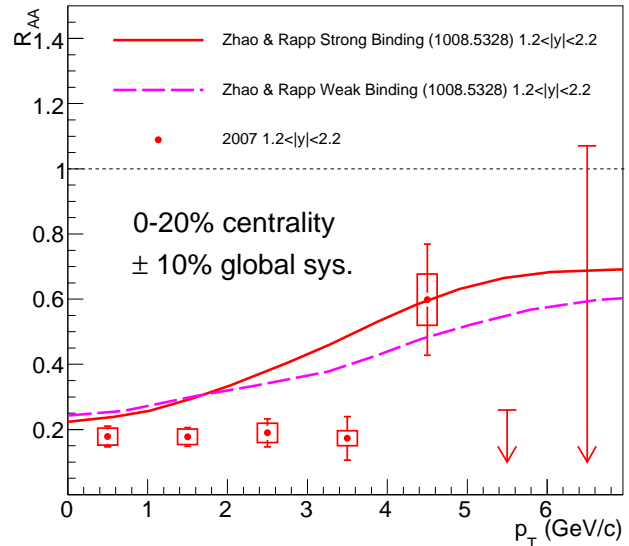


FIG. 10: (Color online) J/ψ R_{AA} as a function of p_T in the 0-20% centrality bin at forward rapidity. Overlaid are a more recent calculation of Zhao and Rapp [30, 31].

contribution. As a result of the ad hoc use of a larger effective absorption cross section at forward rapidity, this new calculation produces a forward to midrapidity R_{AA} ratio of about 0.7 in central collisions, which is in better agreement with the data. Again, this is entirely due to the cold nuclear matter effects, and in fact the hot nuclear matter suppression in this calculation is almost identical between forward and midrapidity.

A second model of interest to the p_T dependence of J/ψ production is the so-called Hot Wind model [33]. This model predicts a decrease in J/ψ R_{AA} at higher p_T in semi-central events, based on a modification of the screening length due to the relative velocity between the J/ψ and the medium. However, there is no quantitative calculation available at forward rapidities, and there is no evidence for such an effect in the p_T range covered by the present data.

IV. SUMMARY AND CONCLUSIONS

We have presented new and more precise measurements of J/ψ nuclear modification at forward rapidity in Au+Au collisions at $\sqrt{s_{NN}} = 200$ GeV. The results confirm our earlier published findings of a larger suppression at forward compared with midrapidity. This, combined with the similar suppression of J/ψ at midrapidity between RHIC and lower energy measurements, remains an outstanding puzzle in terms of a full theoretical description.

Due to the lack of a comprehensive and consistent understanding of the numerous cold nuclear matter effects

and their extrapolation to nucleus-nucleus collisions, extracting a quantitative measurement of the hot nuclear matter effects is not possible at the present time. However, it is clear that the observed suppression is attributable to hot nuclear matter effects, as the suppression in Au+Au collisions is larger than predicted by the

current models of CNM effects. It will be useful for all calculations to include the transverse momentum dependence for future comparisons, especially as the experimental uncertainties, particularly at high p_T , will only improve in the future.

-
- [1] T. Matsui and H. Satz, *Phys. Lett. B* **178**, 416 (1986).
 [2] M. Abreu et al. (NA50 Collaboration), *Physics Letters B* **477**, 28 (2000).
 [3] D. Kharzeev, C. Lourenco, M. Nardi, and H. Satz, *Z.Phys.* **C74**, 307 (1997), hep-ph/9612217.
 [4] U. W. Heinz and M. Jacob (2000), nucl-th/0002042.
 [5] A. Adare et al. (PHENIX Collaboration), *Phys. Rev. Lett.* **98**, 232301 (2007), nucl-ex/0611020.
 [6] J. Nagle (for the PHENIX Collaboration) (2007), 0705.1712.
 [7] H. Pereira Da Costa (PHENIX Collaboration), *Nucl.Phys.* **A774**, 747 (2006), nucl-ex/0510051.
 [8] B. Alessandro et al. (NA50 Collaboration), *Eur. Phys. J. C* **33**, 31 (2004).
 [9] R. Arnaldi (NA60), *Nucl. Phys.* **A830**, 345c (2009), 0907.5004.
 [10] C. Lourenco, R. Vogt, and H. K. Woehri, *JHEP* **02**, 014 (2009), and references therein.
 [11] K. Adcox et al. (PHENIX Collaboration), *Nucl. Inst. and Meth. A* **499**, 469 (2003).
 [12] M. Allen et al. (PHENIX Collaboration), *Nucl. Inst. and Meth. A* **499**, 549 (2003).
 [13] H. Akikawa et al. (PHENIX Collaboration), *Nucl. Inst. and Meth. A* **499**, 537 (2003).
 [14] M. L. Miller, K. Reygers, S. J. Sanders, and P. Steinberg, *Annu. Rev. Nucl. Part. Sci.* **57**, 205 (2007).
 [15] A. Adare et al. (PHENIX Collaboration), *Phys. Rev. C* **77**, 024912 (2008), 0711.3917.
 [16] R. Brun et al., CERN Program Library Long Write-up W5013 (1994), URL <http://wwwasd.web.cern.ch/wwwasd/geant/>.
 [17] A. Adare et al. (2010), 1010.1246.
 [18] A. Milov, W. Anderson, B. Azmoun, C.-Y. Chi, A. Drees, et al., *J.Phys.G* **G34**, S701 (2007), physics/0701273.
 [19] D. Kharzeev, E. Levin, M. Nardi, and K. Tuchin, *Nucl. Phys. A* **826**, 230 (2009), 0809.2933.
 [20] K. Tuchin, *Nuclear Physics A* **854**, 198 (2011), 1012.4212.
 [21] M. Nardi, *Nucl. Phys.* **A855**, 392 (2011).
 [22] A. Capella and E. G. Ferreira, *The European Physical Journal C* **42**, 419 (2005), hep-ph/0505032.
 [23] A. Capella, L. Bravina, E. G. Ferreira, A. B. Kaidalov, K. Tywoniuk, and E. Zabrodin, *Eur. Phys. J. C* **58**, 437 (2008), 0712.4331.
 [24] X. Zhao and R. Rapp, *Phys. Lett. B* **664**, 253 (2008), 0712.2407.
 [25] X. Zhao and R. Rapp, *Eur. Phys. J.* **62**, C109 (2009), 0810.4566.
 [26] J. Nagle, A. Frawley, L. L. Levy, and M. Wysocki (2010), 1011.4534.
 [27] R. L. Thews and M. L. Mangano, *Phys. Rev. C* **73**, 014904 (2006), nucl-th/0505055.
 [28] K. Zhou, N. Xu, and P. Zhuang, *Nucl.Phys.* **A834**, 249C (2010), 0911.5008.
 [29] K. J. Eskola, H. Paukkunen, and C. A. Salgado, *JHEP* **04**, 065 (2009).
 [30] X. Zhao and R. Rapp, arXiv:1008.5328 [nucl-th].
 [31] X. Zhao, private communication.
 [32] D. Antreasyan, J. W. Cronin, H. J. Frisch, M. J. Shochet, L. Kluberg, P. A. Piroué, and R. L. Sumner, *Phys. Rev. D* **19**, 764 (1979).
 [33] H. Liu, K. Rajagopal, and U. A. Wiedemann, *Phys. Rev. Lett.* **98**, 182301 (2007), hep-ph/0607062.